2013

Spectral distribution of excitation-dependent recombination rate in an In0.13Ga0.87N epilayer

K. Jarašiūnas
Vilnius University

S. Nargelas
Vilnius University

R. Aleksiejūnas
Vilnius University

See next page for additional authors

Jarasiunas, K., Nargelas, S., & Aleksiejunas, R., et al. Spectral distribution of excitation-dependent recombination rate in an In0.13Ga0.87N epilayer. Journal of Applied Physics, 113, 103701 (2013).

Spectral distribution of excitation-dependent recombination rate in an $In_{0.13}Ga_{0.87}N$ epilayer

K. Jarašiūnas,[1,a)] S. Nargelas,[1] R. Aleksiejūnas,[1] S. Miasojedovas,[1] M. Vengris,[2] S. Okur,[3] H. Morkoç,[3] Ü. Özgür,[3] C. Giesen,[4] Ö. Tuna,[4,5] and M. Heuken[4,5]
[1]*Institute of Applied Research, Vilnius University, Vilnius 10222, Lithuania*
[2]*Laser Center of Vilnius University, Vilnius 10222, Lithuania*
[3]*Department of Electrical and Computer Engineering, Virginia Commonwealth University, Richmond, Virginia 23284, USA*
[4]*AIXTRON SE, Kaiserstr. 98, 52134 Herzogenrath, Germany*
[5]*GaN Device Technology, RWTH Aachen University, 52074 Aachen, Germany*

(Received 30 November 2012; accepted 13 February 2013; published online 8 March 2013)

Time-resolved optical techniques of photoluminescence (PL), light-induced transient grating (LITG), and differential transmission spectroscopy were used to investigate carrier dynamics in a single 50-nm thick $In_{0.13}Ga_{0.97}N$ epilayer at high photoexcitation levels. Data in wide spectral, temporal, excitation, and temperature ranges revealed novel features in spectral distribution of recombination rates as follows: at low injection levels, an inverse correlation of carrier lifetime increasing with temperature and diffusivity decreasing with temperature confirmed a mechanism of diffusion-limited nonradiative recombination at extended defects. Carrier dynamics in the spectral region below the absorption edge but ~70 meV above the PL band revealed a recombination rate that increased with excitation, while recombination rate in PL emission band (420–430 nm) decreased after saturation of trapping centers. Monitoring of spectrally integrated carrier dynamics by LITG technique allowed us to ascribe the enhanced recombination rate to bimolecular recombination and determine its coefficient $B = 7 \times 10^{-11}$ cm^3/s. Complementary measurements unveiled the cause of PL efficiency saturation at injection levels above 5×10^{18} cm^{-3}, attributable to bandgap renormalization in the extended states above the PL emission band, which encumbers carrier transfer from high-to-low energy states. As the degree of localization, and therefore, the total number of band tail states is expected to increase with In content, their impact to dependence of PL efficiency on excitation density could even be stronger for higher In compositions. These results provided insight that spectrally resolved carrier generation-recombination rates are excitation-dependent and would play a critical role in saturation of internal quantum efficiency in InGaN alloys used in light emitters, such as light emitting diodes. © *2013 American Institute of Physics*. [http://dx.doi.org/10.1063/1.4793637]

I. INTRODUCTION

Study of carrier dynamics in InGaN alloys and heterostructures allows determination of recombination parameters in part in response to the fact that the origin of photoluminescence (PL) efficiency degradation at relatively high optical (electrical) injections still remains an object of studies. This is a rather complicated task due to overlapping effects of carrier localization phenomena, presence of piezoelectric field, carrier leakage, and others in effect. They collectively lead to injection-dependent interplay of radiative and nonradiative recombination rates. Heretofore studies have been undertaken predominantly in InGaN/GaN light-emitting diode (LED) structures to understand "efficiency droop," which has been attributed to impact of Auger recombination, carrier delocalization, electron leakage out of active region, and carrier asymmetry (for a brief review see Refs. 1–4). While the two latter effects seem to be more important for biased device structures, the two former ones may take place under optical carrier injection, when carriers reside mainly in the wells. Consequently, a more detailed study of carrier dynamics with temporal, spatial, and spectral resolution is required to reveal recombination and diffusion processes in InGaN alloys and heterostructures under high injection.

To date, time-integrated (TI) and time-resolved photoluminescence (TRPL) techniques have mostly been used for monitoring radiative recombination pathways and evaluation of internal quantum efficiency in semiconductor heterostructures. The advantage of PL based techniques that provide easy access to spectral features of emission is encumbered by rather vexing interpretation of TRPL decay kinetics as their non-exponential transients vary with injection and temperature because of simultaneous overlapping of different recombination mechanisms (excitonic and free carrier, radiative and nonradiative). A recent study of carrier dynamics in InGaN quantum wells using a number of optical time-resolved techniques has demonstrated the validity of excitation-enhanced nonradiative recombination of delocalized carriers, while the impact of this effect to PL efficiency was not disclosed.[5] Therefore, a deeper insight into any correlation of structural, optical, and photoelectrical

a)Author to whom correspondence should be addressed. E-mail: kestutis.jarasiunas@ff.vu.lt. Tel.: +370 5 2366036. Fax: +370 5 2366037.

properties of nitride semiconductors requires not a single, but several complementary spectrally, spatially, and time-resolved optical techniques for monitoring both the radiative and nonradiative recombination mechanisms, carrier diffusion, and features of these processes in a wider spectral region than the PL does, which is the subject matter of the present manuscript.

Defect-insensitive emission has been intensively studied mainly in quantum well structures of InGaN,[6,7] wherein many factors contribute to enhancement of PL efficiency (localization of holes and probably electrons at nanometer scale, screening of quantum-confined Stark effect, QCSE). At the same time, highly defective thick epitaxial InGaN films (where polarization field is negligibly weak and indium fluctuation at the few nanometer scale is unlikely) also exhibited high PL efficiency[8] and long nonradiative carrier lifetimes.[9] In these quasi-bulk layers, studies of carrier dynamics have been limited, while their investigation may clarify impact of larger scale inhomogeneities to PL efficiency enhancement and its gradual loss at high injections.

Therefore, in this work, we focused on a detailed study of carrier dynamics in a single InGaN layer. We applied linear and nonlinear optical techniques to investigate excitation-dependent recombination rates in a 50-nm thick epitaxial layer of $In_{0.13}GaN$ alloy. Time-integrated and time-resolved photoluminescence (TRPL) spectroscopy allowed measurement of PL efficiency as well as PL decay kinetics at various injected carrier densities. By exploring time-resolved differential transmission (DT) spectra, the narrow spectral range accessible by PL was extended well above the lowest band tail states of InGaN alloy. Light-induced transient grating (LITG) technique was used to probe spectrally integrated carrier dynamics with spatial and temporal resolution, thus providing directly the values of carrier lifetime and diffusion coefficient. Consequently, a full set of data from complementary optical techniques provided excitation energy density, spectral position, and temperature dependent recombination rates in the epitaxial InGaN layer, allowed direct determination of the bimolecular recombination coefficient, and unveiled causes of efficiency saturation of the main PL emission band.

II. SAMPLE AND TECHNIQUES

A 50-nm thick $In_{0.13}Ga_{0.87}N$ epilayer was grown on a few-micrometer thick GaN-on-sapphire template by using AIXTRON 3×2 Close-Coupled Showerhead reactor. A substrate temperature of 732 °C and a chamber pressure of 200 mbar were used for InGaN growth. Structural properties and the strain were studied by means of X-ray diffraction (XRD), rocking curve, and reciprocal space mapping (RSM) of (10–15) reflection, respectively. Atomic force microcopy (AFM) was used for surface morphology investigation. The In content of the layer was determined through XRD ω-2θ measurement with the aid of simulations. The XRD spectra exhibited a sharp InGaN peak with very clear Fabry-Pérot interfaces and with a narrow full width at half maximum (FWHM) of 400 arcsec for the symmetric diffraction of (0002) revealing the high crystal quality of the InGaN layer. RSM confirmed that the InGaN layer is fully strained. Simulation of XRD data yielded an In content of 13%. The strain state of the InGaN layer was taken into consideration during the simulation of XRD ω-2θ scan in order to achieve reliable In content. The AFM measurements revealed a surface morphology dominated by terraces with a roughness of 0.8 nm and V-pits with density of about $2.5 \times 10^8\,cm^{-2}$. The latter value for InGaN is comparable with that in GaN layers, suggesting that not many dislocations are formed at the InGaN/GaN interface which propagate through the InGaN layer and manifest themselves as V-pits on the surface.

A standard PL spectroscopy setup was employed using ~150 fs pulses at 375 nm wavelength (the 2nd harmonic of an 80 MHz repetition rate Ti-Sapphire laser) for selective excitation of the InGaN layer. Using a spectrometer and a Hamamatsu streak camera, PL spectra and kinetics were measured for injected carrier densities in the range of $\sim 10^{16}$ to $10^{18}\,cm^{-3}$. To reach higher injections, e.g., up to $5 \times 10^{19}\,cm^{-3}$, another setup with 20 ps pulse duration at 266 nm (model PL2143, Ekspla) was used. In the latter setup, TRPL measurements with 25 ps temporal resolution were performed using a Kerr shutter with toluene.

The experimental setup for time-resolved DT is based on a commercial Ti:Sapphire femtosecond amplifier (SuperSpitfire, Spectra Physics) delivering 800 nm pulses of 120 fs duration at 1 kHz repetition rate. The output of the amplifier was split into two equal parts. One was used to pump the optical parametric amplifier (TOPAS, Light Conversion) that provided 120 fs pulses set to 330 nm wavelength (3.75 eV). The second beam was delayed and used to generate white light continuum in a CaF_2 window. The DT technique provided means to observe evolution of DT spectra in 380–480 nm range with high temporal resolution.

LITG technique explores for excitation an interference pattern of two coherent beams of a YLF:Nd^{3+} laser (PL2243, Ekspla) emitting 8 ps duration pulses at 1053 nm or a YAG:Nd^{3+} laser (PL2243, Ekspla) emitting 25 ps duration pulses at 1064 nm. The 3rd or 4th laser harmonics were used for recording the transient spatially modulated free carrier pattern $N(x) = N_0 + \Delta N(1 + \cos[2\pi x/\Lambda])$ with spacing Λ, which modulates the refractive index $\Delta n(x) \propto \Delta N(x)$ and diffracts a delayed probe beam at 1053 nm. Diffraction efficiency of the grating, η, and its decay, $\eta(t) = (2\pi\, n_{eh} \Delta N d/\lambda_{probe})^2 \exp(-2t/\tau_G)$, where n_{eh} is the refractive index change per one electron-hole pair and d is the layer thickness, provided a convenient way to discriminate the recombination-governed grating decay time τ_R and the diffusive decay time τ_D, according to the relationship $1/\tau_G = 1/\tau_R + 1/\tau_D$. Measurements of grating period Λ dependent diffusive decay time $\tau_D = \Lambda^2/(4\pi^2 D_a)$ were used for determination of the bipolar diffusion coefficient D_a.[10] The measurements were performed at various photoexcited carrier densities ($\sim 10^{18}$–$5 \times 10^{19}\,cm^{-3}$) and temperatures (80 to 300 K).

III. RESULTS AND DISCUSION

A. Characterization by PL techniques

Time-integrated room-temperature PL spectra were measured at low excitations ($I_0 \sim$ 6–10 $\mu J/cm^2$) using selective

excitation at 375 nm (150 fs pulses) or at 266 nm (25 ps pulses). The emission line for the InGaN alloy with 13% In content was positioned at 424 ± 6 nm at FWHM (2.922 ± 0.040 eV). TRPL kinetics at relatively weak selective excitation of the InGaN layer (in the 10^{16} to 10^{18} cm^{-3} range) revealed increasing PL decay times with increasing injection (Fig. 1), thus indicating a gradual saturation of nonradiative recombination centers. This tendency was also verified by a change of the power index, β, of PL intensity dependence on excitation density, $I_{PL} \propto I_0^{\beta}$. Its plot in log-log scale (Fig. 2) revealed the change from $\beta = 2.7$ to $\beta = 2$ at a carrier density of 10^{17} cm^{-3} at room temperature. After the saturation of trapping centers, the nonradiative carrier lifetime became constant and PL intensity increased quadratically with injection ($\beta = 2$). The latter β value is indicative of the fact that the injected electron and hole density $N_{e,p}$ is larger than the residual electron concentration n_0, thus $N_e = N_p > n_0$ and PL intensity increase follows the relationship $I_{PL} \propto (n_0 + N_e)N_p \propto I_0^2$. We note that at 10 K, the change of index β (from ~1.5 to 1, see Fig. 2) takes place also at the same carrier density as for RT (i.e., after the trapping centers—the residual acceptors with density of about 10^{17} cm^{-3} become saturated). At these conditions, two factors ensured the radiative PL emission being dominant: (i) the coefficient of radiative recombination B essentially increases at low temperatures ($B \propto 1/T^{3/2}$)[11] and (ii) excitonic nature of emission dominates due to relatively high exciton binding energy, leading to $I_{PL} \sim B_{ex} n_{ex}$ (Ref. 12) and thus providing the typical $\beta = 1$ slope value.

Excitation of the sample by picosecond pulses at 266 nm wavelength enabled us to reach excess carrier peak densities up to 10^{20} cm^{-3}. At these high-excitation conditions, the backscattered PL spectra revealed only the features of spontaneous emission, while the underlying GaN layer showed both the spontaneous (at ~3.4 eV) and stimulated emission (SE) at ~3.32 eV. The absence of a clear SE peak from InGaN layer is typical for luminescence in case of spatial fluctuations of In content,[13] thus only a slight narrowing of the emission peak above a threshold density of 0.33 mJ/cm^2 was observed. Nevertheless, a very fast decay transient of PL (temporal shape of which repeated the laser pulse) confirmed the presence of SE. Further measurements of InGaN luminescence were performed using thin stripe excitation and edge emission detection.[13] The dependence of PL intensity on excitation (Fig. 3) revealed the presence of SE with its threshold at $I_0 \approx 0.1$ mJ/cm^2. The increase of β up to 3.7 was observed at an excitation density above the SE threshold, while further increase in excitation led to saturation of luminescence intensity due to limited number of excited states.

Knowledge of the SE threshold allowed us to limit the further measurements of carrier dynamics in InGaN epilayer up to this level (0.1 mJ/cm^2), until the non-equilibrium processes reveal the peculiarities of spontaneous emission. We present below investigation of the recombination and transport features by using techniques of DT and LITGs.

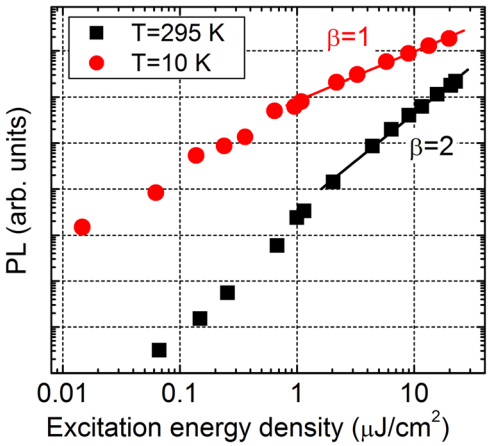

FIG. 2. Dependence of time-integrated PL intensity on excitation energy density using femtosecond pulses at 375 nm. The curves can be approximated by a power-function $I_{PL} \sim I_0^{\beta}$ with slope values β, as indicated on the plot.

B. Differential transmission spectroscopy

The PL spectroscopy allows access only to the limited spectral region of radiative emission from localized states,

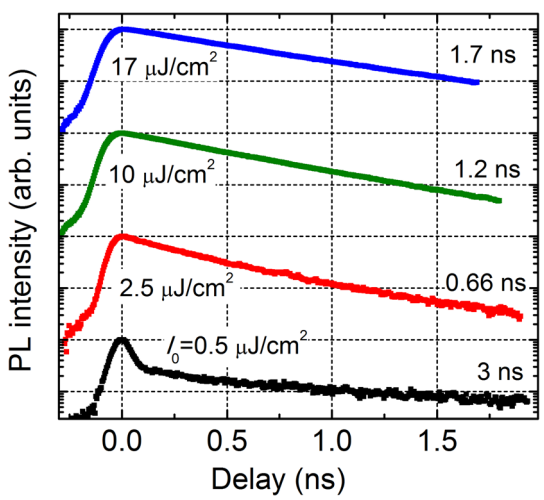

FIG. 1. PL decay kinetics measured using femtosecond pulses at 375 nm wavelength and various excitation densities I_0, corresponding to injected carrier densities from 5×10^{16} to 10^{18} cm^{-3}.

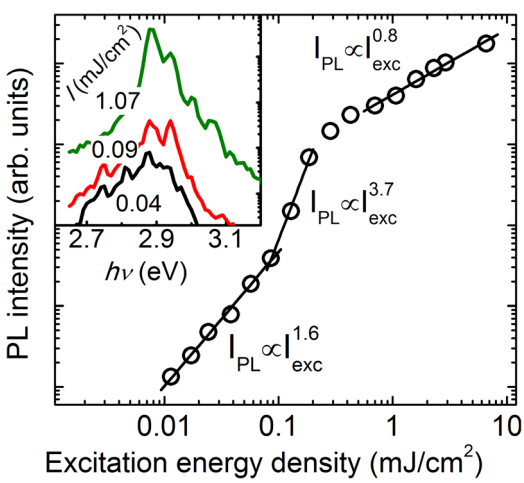

FIG. 3. Dependence of time-integrated PL intensity on excitation energy density using edge emission geometry. PL spectra at injection levels below and above SE threshold are given in an inset.

while a large Stokes shift in InGaN epilayers and QWs, linearly increasing with In content[14] suggests that there is a broad spectral distribution of localized and extended states. For the $In_{0.13}GaN$ layer investigated here, a 125 meV Stokes shift is expected.[14] Consequently, the emission peak at 2.922 eV predicts an effective bandgap energy of $E_B \approx 3.05$ eV for this alloy. As PL emission originates from the lowest energy states near the band tail, where the density is lower than that in the extended states, the spectrally and temporally resolved DT measurements are needed to reveal the excitation relaxation dynamics of all available states, and especially of the states above the mobility edge, which will be occupied after filling the band tail states under strong excitation conditions (but still below the SE threshold).

To explore the full spectral range and determine spectrally dependent relaxation rates, we performed spectrally and temporally resolved DT measurements in wide spectral (390 to 440 nm) and excitation range (4 to 520 μJ/cm^2). In Fig. 4, we present DT spectra measured at 10 ps and 1 ns after photoexcitation. The DT spectra are blue shifted with respect to those obtained by PL. This shift is ascribed to relatively larger density of higher energy states contributing to the absorption bleaching. The FWHM of DT spectra is rather narrow (~60 meV), but it broadens towards the blue energy wing due to temporary filling of extended states at higher excitations. The spectral broadening is followed by faster relaxation rates, and the DT spectra become symmetric after 1 ns (Fig. 4). Spectrally integrated DT kinetics within 390–440 nm range exhibit faster decays with increasing excitation fluence (I_0). The fast decay transient lasts only 1–2 ns and follows $1/I_0$ dependence, thus indicating shorter average carrier lifetimes in higher energy extended states than in the lower ones. The question then is whether the increasing decay rate is caused by transfer of delocalized and thus more mobile carriers to lower energy states or whether it is due to

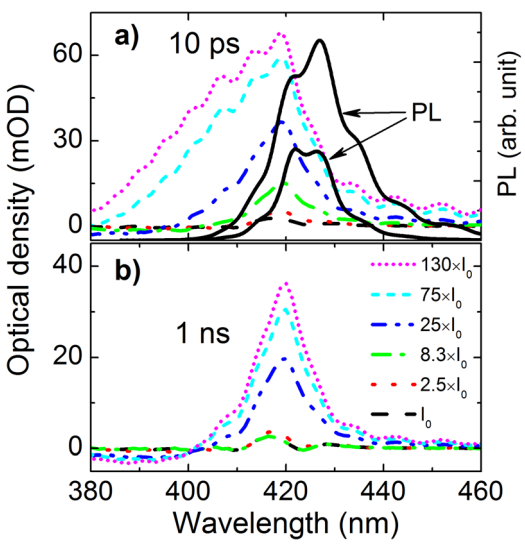

FIG. 4. DT spectra at various excitation energy densities I_0 (here $I_0 = 4\ \mu$J/cm^2). The spectra are taken at 10 ps (a) and 1 ns (b) after photoexcitation by 200 fs duration laser pulses at 375 nm. For comparison, PL spectra at 20 μJ/cm^2 (375 nm excitation) and 100 μJ/cm^2 (266 nm excitation) are shown in (a).

increasing recombination rate in extended states with excitation. In order to entertain an answer, we determined decay times of DT spectral components as well as their injection-dependences. In Fig. 5, we present spectrally resolved DT kinetics at various excitation energy densities (in the range from 10 to 300 μJ/cm^2) for two spectral positions, corresponding to the central line of PL peak (425 nm) and of DT blue wing (414 nm). In the spectral range of PL, the low-injection DT decay is fast but slows and saturates with excitation, exhibiting $\tau_{DT} = 1.5$ ns decay time (similarly to PL decay times at RT, see Fig. 1). Despite the fact that the DT measurements were performed at excitation energy densities up to 300 μJ/cm^2 (i.e., by more than an order of magnitude higher than the selective photoexcitation of PL up to 17 μJ/cm^2), the DT kinetics did not reveal any faster recombination transient at 425 nm, which would confirm the PL radiative recombination being dominant. The observed long DT decay at the blue wing (at low excitations τ_{DT} equals to 6–8 ns, which is 10-times longer with respect to DT decay in the PL window) does not support the common tendency of increasing PL decay rate at the high energy wing. Moreover, the DT decay time at the blue wing decreases with injection in the 30–100 μJ/cm^2 range. Fig. 5(c) summarizes the variation of carrier lifetimes in the spectral range from the PL emission band up to absorption edge and their dependence on injected carrier density. The data clearly show that the spectral interval of ~415 nm (i.e., ~70 meV above the PL peak) is favorable for carrier accumulation at low injections. Consequently, prolonged carrier lifetime in the blue-wing of extended states and their subsequent faster decay at higher injections may strongly impact the PL characteristics indirectly. Namely, at low injections, this wing plays the role of a reservoir to accumulate injected carriers to be transferred to the lower energy states responsible for the PL emission, while at higher injections the fast recombination rate in this wing consumes the carriers locally and diminishes their delivery to the PL band most likely due to bandgap renormalization, as will be discussed below. It is worth to note that the injection-enhanced DT decay at blue wing starts at $I_0 = 20$–$33\ \mu$J/cm^2 (5×10^{18} cm^{-3}) (as can be seen both in spectrally resolved kinetics (Figs. 5(a) and 5(b) and spectrally integrated ones) and lasts for about 1 ns, while at later times it slows to values typical for low-injection (6–8 ns for $N \leq 10^{18}$ cm^{-3}). As the DT technique in the vicinity of absorption edge monitors the overall decay rate, which is equal to the sum of the recombination rate and carrier transfer rate to the lower energy states,[15] it is difficult to judge about the mechanism for enhanced decay rate in the blue wing. In general, the faster decay at high injection is attributed to increasing radiative recombination rate of localized carriers or excitons (especially in QWs[16]). Hypothesis of excitation-enhanced defect related recombination has also been provided[4] within the framework of carrier delocalization in QWs. Moreover, screening of the potential barriers around deep charged defects[7] at high injections may reduce the effective barrier for diffusive carrier flow to electrically active dislocations. Therefore, for a deeper understanding of carrier-density dependent effects in InGaN alloy, we performed complementary measurements of carrier recombination and diffusivity in

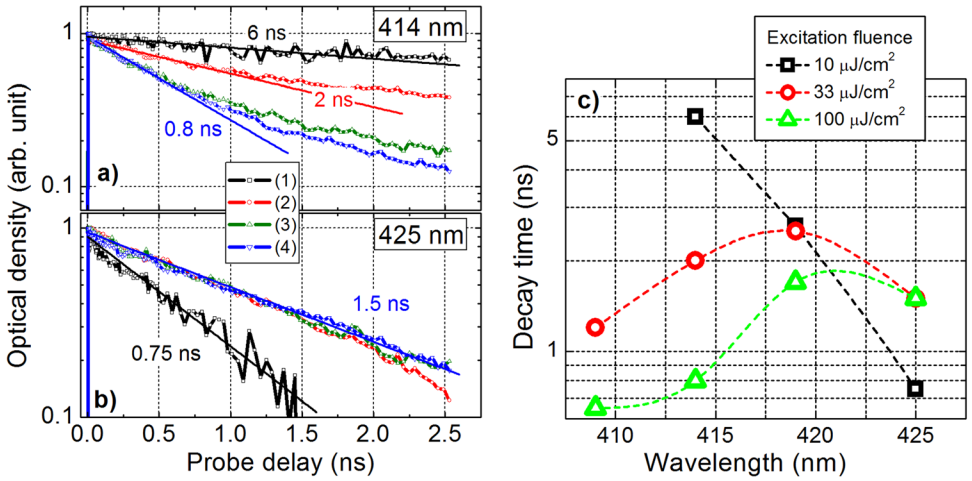

FIG. 5. Spectrally resolved DT kinetics (a), (b) for two spectral lines which correspond to blue wing of DT at 414 nm and PL emission at 425 nm at various excitation energy densities $I_0 = 10\,\mu$J/cm^2 (1), 33 μJ/cm^2 (2), 100 μJ/cm^2 (3), and 300 μJ/cm^2 (4). In (c), spectral distribution of the initial DT decay time is plotted for various I_0.

a wide excitation and temperature range, using the picosecond LITG technique.

C. Characterization by LITGs

Time-resolved LITG technique allows direct monitoring of excess carrier dynamics and determination of excitation-dependent carrier recombination rates. It provides nonresonant probing of light-induced refractive index modulation, Δn, at wavelength well below the bandgap (1064 nm).[17] Under these conditions, linear dependence of Δn on spectrally integrated nonequilibrium carrier density ΔN makes the analysis of LITG characteristics relatively simple.[18] The probe beam diffraction efficiency η of the TG depends quadratically on injected carrier density, $\eta \propto \Delta N^2 \exp(-2t/\tau_G)$. Single exponential kinetics of LITG at various grating periods allow determination of the carrier lifetime τ_R and diffusion coefficient D. If, however, the lifetime or diffusivity is dependent on carrier density, the grating decay becomes nonexponential.[19] Another measurable characteristic is the dependence of grating diffraction efficiency η on the excitation energy density, $\eta \propto I_0^{\gamma}$. The latter dependence is a power function with the index value γ, which equals to 2 at linear generation and recombination rates. However, excitation-dependent changes in carrier generation or recombination rates will lead to change of the index value.[20]

Decay kinetics of LITG (at $\Lambda = 12\,\mu$m) for excitation energy densities in the range of 10–300 μJ/cm^2 revealed a nearly single exponential decay with a characteristic time $\tau_G = \tau_R = 1.55$ ns only at the lowest injection used (10 μJ/cm^2). At higher excitation levels (above 5×10^{18} cm^{-3} at the front surface of the layer), the fast decay transient emerges in 1–2 ns time interval characterizing the excitation-enhanced recombination rate. At $I_0 = 300\,\mu$J/cm^2, a very fast decay component appears, which follows the laser pulse of width 25 ps, thus indicating stimulated decay of emission (SE). The latter feature was also observed in PL decay at similar injection levels.

Comparison of excitation dependences for InGaN/GaN layers at various delay times Δt (Fig. 6) revealed some important features in injection-dependent recombination rate. For the InGaN layer under investigation, gradually decreasing index value γ in the $I_0 = 10$–$100\,\mu$J/cm^2 range points out that the carrier lifetime in InGaN becomes dependent on injected carrier density. In contrast, the index value $\gamma = 2$ for underlying GaN layer (in the range of $I_0 = 0.4$–1 mJ/cm^2) remains constant up to the threshold of stimulated emission (5×10^{19} cm^{-3}). This behavior has been observed in other metalorganic chemical vapor deposition (MOCVD)-grown GaN layers as well[21] and can be explained as follows: the radiative recombination rate $\tau_{Rad} = 1/BN$ in GaN increases with excess carrier density, but its impact is masked by a faster nonradiative recombination rate. Thus, more sensitive response of InGaN layer to the excitation suggests a higher radiative recombination rate and requires numerical modeling of carrier dynamics.

In order to carry out the abovementioned numerical modeling, the excess carrier density and the absorption coefficient at 355 nm for the InGaN layer are needed. The latter was determined from the measured dependence of η (I_0) (Fig. 6). Here, the diffraction efficiency from InGaN layer saturates near the SE threshold, and the subsequent increase of η at $I_0 > 300\,\mu$J/cm^2 is due to contribution of the grating recorded in the underlying 2 μm-thick GaN layer (we note that the diffraction efficiency from the GaN layer, η_{GaN}, also

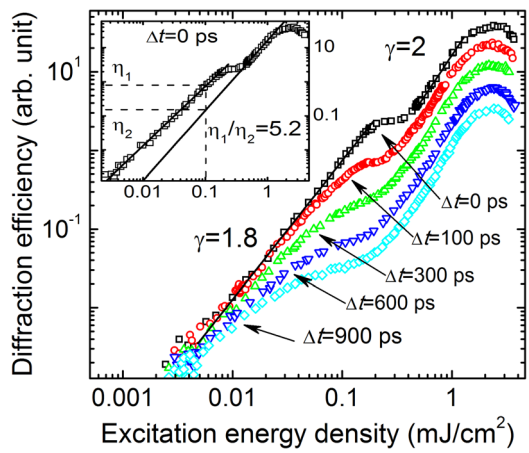

FIG. 6. Dependence of diffraction efficiency η on excitation energy density I_0 for different delay times Δt of a probe beam. The dependence at $\Delta t = 0$ can be approximated by a power function $\eta \propto I_0^{\gamma}$ with slope value γ, as indicated in the plot. An inset shows enlarged view of η (I_0) for comparison of η values from the InGaN layer (η_1) and GaN layer (η_2).

saturates when the SE threshold of 1.5 mJ/cm^2 is reached). Extrapolation of $\eta_{GaN}(I_0)$ to the low injection range (see the solid line in the inset of Fig. 6) characterizes the ratio of diffraction efficiencies from both InGaN and GaN layers ($\eta_{InGaN}/\eta_{GaN} = \eta_1/\eta_2 = 5.2$) as well the ratio of excess carrier densities ($N_{InGaN}/N_{GaN} = 2.3$), integrated over the depth of the layer. From these results, an absorption coefficient of 1.6×10^5 cm^{-1} was calculated at 355 nm and used for calibration of the excess carrier density in InGaN: for $I_0 = 10\,\mu$J/cm^2, N_{InGaN} is equal to 2×10^{18} cm^{-3} at the front surface of the layer.

A deeper insight into the enhanced recombination mechanisms requires measurements of temperature-dependent recombination rate and diffusivity in the InGaN layer. The LITG decay was measured at small grating periods to ensure diffusive grating decay and determine the values of D and lifetime τ_R at carrier densities as low as 2×10^{18} cm^{-3}. An inverse correlation between the decreasing bipolar diffusion coefficient ($D \propto T^{-1/2}$) and increasing lifetime with T ($\tau_R \propto T^{1/2}$) is observed (Fig. 7(a)), confirming that the nonradiative lifetime values of 0.15–1 ns in the 50 nm thick InGaN layer are determined by carrier diffusion to dislocations and associated point defects. Similar mechanism of diffusion-limited recombination rate was observed in hydride vapor phase epitaxy-grown GaN layers, leading to nonradiative carrier lifetimes in range from 0.4 to 40 ns at 300 K[10,22]). We note that the typical recombination rate via point defects would follow the relationship $1/\tau_R \propto T^{1/2}$, according to Shockley-Read-Hall (SRH) recombination model: $1/\tau_R = N_T \sigma v_{th}$, where $v_{th} \propto T^{1/2}$. The observed opposite tendency in the investigated InGaN layer strongly supports the dominant role of extended defects, as centers of nonradiative recombination. As for the mobility, its temperature dependence followed the well-known relationship $\mu \propto T^{-1.45}$, confirming the mechanism of carrier scattering by acoustic phonons. At half injection level (30 μJ/cm^2), the decreased power index ($\mu \propto T^{-1.2}$) indicates contribution of additional scattering, presumably by charged defects. Our observations suggest that screening of charged defects at relatively higher injection levels may lead to enhanced diffusivity, and thus to shorter nonradiative lifetimes (according to the dependence displayed in Fig. 7). Note that we experimentally observed decreasing lifetimes with excitation at RT (Fig. 8) but not an increase of D vs. N (Fig. 7(b)). Absence of the latter dependence is probably due to compensation by a more dominant effect such as the bandgap renormalization (BGR), which is the strongest in the induced grating peaks and spatially modulates the bandgap ΔE_g, thus diminishing the D value (ΔE_g may reach 18 meV in GaN at 10^{19} cm^{-3} (Ref. 10)). On the other hand, increase of both carrier diffusivity and bimolecular recombination rate may take place when the degenerate plasma density limit is reached.[19]

D. Determination of InGaN bimolecular recombination coefficient

Contribution of bimolecular recombination was analyzed by numerical fitting of the experimentally measured set of LITG decay kinetics at various injected carrier densities (Fig. 8) and temperatures in the 10–300 K range (Fig. 9). For modeling of spatial and temporal carrier distribution, we refer to the continuity equation[23]

$$\frac{\partial N(x,z,t)}{\partial t} = D(\Delta N)\nabla^2 \Delta N(x,z,t) - A\Delta N(x,z,t) - B\Delta N^2(x,z,t) + G(x,z,t), \quad (1)$$

where $G(x, z, t) = \alpha I_0(1 - R)\exp(-\alpha z)$ is the carrier generation rate in InGaN layer, D is the ambipolar diffusion coefficient, $A = 1/\tau_R$ and B are the SRH and bimolecular recombination coefficients. The required modeling parameters $1/\tau_R(T)$ and $D(T)$ for the investigated InGaN layer were measured at low injections (Fig. 7(a)), and the absorption coefficient $\alpha = 1.6 \times 10^5$ cm^{-1} at the excitation wavelength of 355 nm was determined as described above from the data in Fig. 6. Therefore, only one adjustable parameter, B, was used to fit the sets of LITG decay rates. Numerical solution of $N(x, z, t)$ was used to calculate instantaneous profiles of $\Delta N(z, t)$ and diffraction efficiency $\eta(t) = \int \Delta N^2(t) dz$, which in turn was experimentally measured. The data of $\eta(t)$ vs I_0 provided $B = 7 \times 10^{-11}$ cm^3/s value at RT and its temperature dependence $B \propto 1/T^{3/2}$ in 100–300 K range. The determined B value is slightly larger than that for bulk GaN ($B = 2$–5×10^{-11} cm^3/s) but very close to those for InGaN quantum wells ($B = (7$–$10) \times 10^{-11}$ cm^3/s) with 10% of In.[16,24] The decreased value of B at $T < 100$ K (see inset in Fig. 9) can be a consequence of many-body effects in high-density carrier plasma which are more pronounced at low temperatures and may lead to saturation of radiative recombination rate at densities above 10^{18} cm^{-3}.[16,25]

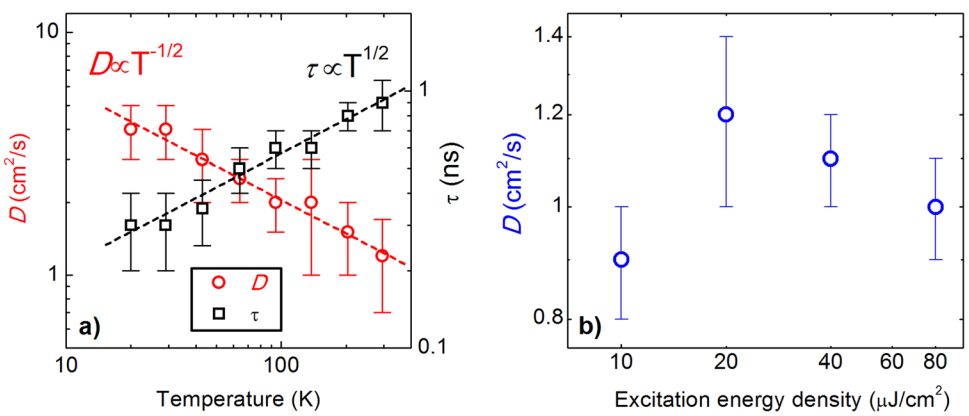

FIG. 7. (a) Temperature dependences of diffusion coefficient D and lifetime τ_R in InGaN layer at excess carrier density $\Delta N = 2$–3×10^{18} cm^{-3} and (b) dependence of D on excitation energy density I_0 (here, average excess carrier density at $I_0 = 10\,\mu$J/cm^2 corresponds to $N = 2 \times 10^{18}$ cm^{-3} for used 266 nm excitation wavelength).

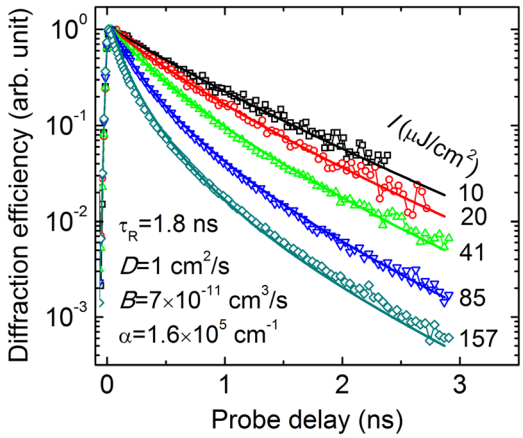

FIG. 8. LITG decay kinetics in InGaN layer at various excitation energy densities I_0, which extend over the excess carrier density range from 2×10^{18} to $3.2 \times 10^{19}\,\mathrm{cm}^{-3}$ (symbols) and their numerical fitting (lines) using parameters given in the legend.

E. Analysis of carrier dynamics measured by different techniques

To reiterate measurements by TRPL and DT techniques under selective excitation of InGaN layer allowed comparison of nonequilibrium processes in various spectral regions below the absorption edge. Let us discuss first the processes in the PL spectral window, which are commonly investigated for evaluation of the internal quantum efficiency. Gradual saturation of the nonradiative recombination centers at injections up to $30\,\mu\mathrm{J/cm}^2$ was verified by longer decay times of PL and DT @425 nm (nevertheless, $\tau_{\mathrm{NonRad}} \ll \tau_{\mathrm{Rad}}$ remained valid). The decreased nonradiative recombination rate was favorable for increase of PL efficiency up to the threshold of stimulated emission, while the PL increase was linear up to $20\,\mu\mathrm{J/cm}^2$ (Fig. 2) and sublinear up to SE threshold (Fig. 3). It is important to note that DT@425 nm decay time of 1.5 ns saturated at $I_0 = 30\,\mu\mathrm{J/cm}^2$ (i.e., at a similar level as that for PL) and did not decrease with increasing excitation energy density up to $I_0 = 300$–$520\,\mu\mathrm{J/cm}^2$. Under these conditions, the estimation based on the determined value of $B = 7 \times 10^{-11}\,\mathrm{cm}^3/\mathrm{s}$ and excess carrier density of 3–$5 \times 10^{19}\,\mathrm{cm}^{-3}$ resulted in $\tau_{\mathrm{Rad}} = 1/BN = 0.3$–$0.6$ ns and, thus, predicted the subnanosecond DT@425 nm decay time at 300–520 $\mu\mathrm{J/cm}^2$: $\tau_{\mathrm{DT}} = (1/\tau_{\mathrm{NonRad}} + 1/\tau_{\mathrm{Rad}})^{-1}$. This discrepancy calls for the need for a more explicit approach to evaluate the spectral density of excess carriers at excitations above $30\,\mu\mathrm{J/cm}^2$. After filling of the lowest states in the conduction and valence bands (this is clearly seen from DT broadening towards the high-energy wing in Fig. 4(a)), the absorbed fluence starts to create carriers in a much wider spectral range. Therefore, generation rate to PL spectral window is expected to decrease gradually with excitation. To verify this premise, we compared dependences of DT signal on excitation density ($I_{\mathrm{DT}} \propto I_0^{\gamma}$, Fig. 10), spectrally integrated over the PL spectral range (420–430 nm, $\mathrm{DT_{PL}}$) and over all the spectral range of photoexcited states (390–430 nm, $\mathrm{DT_{full}}$).The decreasing ratio of $\mathrm{DT_{PL}/DT_{full}}$ at $I_0 > 33\,\mu\mathrm{J/cm}^2$ ($\Delta N > 6.7 \times 10^{18}\,\mathrm{cm}^{-3}$) pointed out to decrease in carrier density available for PL emission, which may cause the gradual saturation of PL intensity vs. excitation. Comparison of the calculated $\mathrm{DT_{PL}}$ integral with experimentally measured dependence of PL intensity on excitation energy density (Fig. 2) discloses rather similar features such as the initial steep increase of I_{PL} with excitation (due to trap saturation), then quadratic increase of PL ($\beta = 2$ in Fig. 2, which corresponds to the linear growth of $\mathrm{DT_{PL}}$),[26] and the ongoing slower growth $I_{\mathrm{PL}} \propto I_0^{1.5}$ at high injections (Fig. 3).

The observed decrease in the carrier generation rate in the spectral region of PL emission is critical for understanding the origin of PL saturation at high injections, i.e., what eventually leads to lower internal quantum efficiency (IQE) values. This drawback is a consequence of nonequilibrium processes in extended states above the PL emission band, which are expected to transfer the photoexcited carriers without significant losses to the lower energy PL states. The reason that the carriers cannot be transferred efficiently to the PL states is probably hidden in the BGR for the occupied higher energy states: as the BGR effect grows with excitation, an additional potential barrier is built and adds to the likely existing potential fluctuations (thus blocking carrier transport to lower energy states). Assuming that holes are

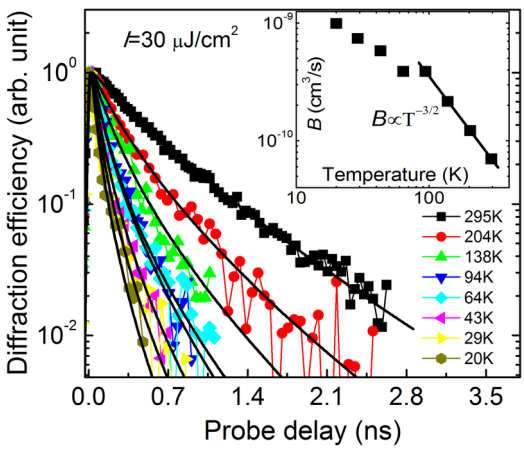

FIG. 9. Temperature-dependent LITG decay kinetics (symbols) at $N = 4 \times 10^{18}\,\mathrm{cm}^{-3}$ and their fitting (lines) using $\mathrm{B} \propto T^{-3/2}$ dependence. The fitting provided value of $\mathrm{B}\,(300\,\mathrm{K}) = 7 \times 10^{-11}\,\mathrm{cm}^3/\mathrm{s}$.

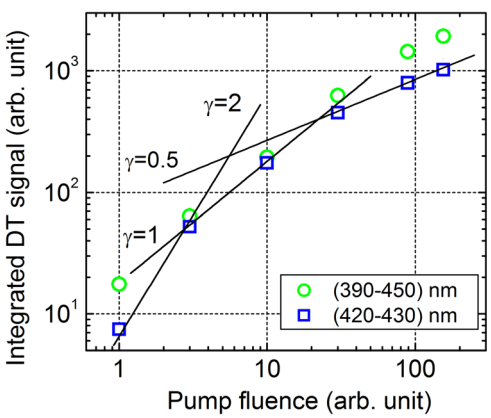

FIG. 10. Dependence of spectrally integrated DT signal I_{DT} on excitation energy density. The slope values γ correspond to approximation by a power function $I_{\mathrm{DT}} \propto I_0^{\gamma}$ and are in relation with slope values β of $I_{\mathrm{PL}} \propto I_0^{\beta}$ dependence as $\gamma = \beta/2$. DT spectra are taken at 10 ps after photoexcitation, thus impact of recombination to DT value and slope is negligible.

strongly localized in the InGaN alloy[7,27] and their decreased diffusivity D_h limits the bipolar diffusion coefficient, $D_a \approx 2D_h$, we can estimate a value of the valance band renormalization according to the following relationship:[28]

$$\Delta E_v(\Delta N) = Z \times [3\,\text{meV}(\Delta N/10^{18})^{1/3} + 19\,\text{meV}(\Delta N/10^{18})^{1/4}] \quad (2)$$

with a material dependent parameter $Z = 0.48$ for GaN.[10] The renormalization value ΔE_v varies from 13 to 23 meV for injected carrier density $\Delta N = 2 \times 10^{18}$–$2 \times 10^{19}\,\text{cm}^{-3}$ and adds to the initial localization energy. The impact of BGR is proved by decreasing with injection carrier diffusivity (see $D_a \approx 1\,\text{cm}^2/\text{s}$ within the interval $I_0 = 20$–$80\,\mu\text{J/cm}^2$ in Fig. 7(c)) while in highly excited GaN epilayer the D_a value doubles with excitation (from 1.5 to ~3 cm^2/s (Ref. 19)).

The above described observations of spectrally dependent diffusivity and recombination rate seem feasible as the higher energy states (regions with lower In content) are *spatially* displaced from the lowest energy states (regions with high In content) and—what is upmost important—the photoexcitation creates very strong potential barrier between these regions, which are retained up to SE threshold. This peculiarity allows carriers to be bunched in spectral region 415–420 nm and recombine here without transfer to the PL band. This is very different from the low injection regime, which does not block the injected carrier transfer from the high energy wing of PL to the low energy states, leading to enhanced PL efficiency.

IV. CONCLUSIONS

Complementary studies of spectral and spatial carrier dynamics in wide excitation and temperature ranges revealed novel features in recombination rates and diffusivity in an InGaN epilayer. We found an inverse correlation, i.e., a carrier lifetime increasing with temperature and a diffusivity decreasing with temperature, which confirmed a mechanism of diffusion-limited nonradiative recombination at extended defects. At higher injections, monitoring of spectrally integrated carrier dynamics by transient gratting technique allowed us to ascribe the enhanced recombination rate to bimolecular recombination and determine its coefficient $B = 7 \times 10^{-11}\,\text{cm}^3/\text{s}$ at room temperature. Increase of carrier recombination rate and decrease of diffusivity in the spectral interval above the PL emission band (415–420 nm), observed by differential transmittivity and transient grating techniques, was attributed to bandgap normalization effect in extended states. Impact of bandgap normalization increased with excitation, building an additional potential barrier for carriers in addition to the already existing potential fluctuations. In this scenario, carrier transfer from high-to-low energy states is inhibited and even blocked, leading to efficiency saturation of the PL band (420–430 nm) at injection levels above $5 \times 10^{18}\,\text{cm}^{-3}$. Based on these complementary results, we underscore the importance of spectrally dependent carrier generation rate which unveiled the causes for efficiency saturation of the main PL emission band in 3D InGaN layer. The latter effect of saturation is seen already at 10 ps after photoexcitation in spectrally integrated DT signal, which in fact reflects the excitation dependence of PL band. The higher the In content, the larger the Stokes shift is, i.e., the higher the number of localized states available for the injected carriers. Consequently, these localized states may have a stronger excitation-dependent impact on radiative emission, resulting in lower PL efficiency as the In composition increases. Similar studies of PL efficiency together with spatial, spectral, and temporal carrier dynamics in InGaN quantum wells may provide deeper understanding of processes leading to saturation of internal quantum efficiency of LEDs.

ACKNOWLEDGMENTS

The work at VU was supported by the European Social Fund and Lithuanian Science Council (Grant No. VP1-3.1-ŠMM-07-K-02-006). VCU team acknowledges support from NSF (Grant No. EPMD 1128489).

[1]Ü. Özgür, H. Liu, X. Li, X. Ni, and H. Morkoç, Proc. IEEE **98**, 1180 (2010).
[2]J. Piprek, Phys. Status Solidi A **207**, 2217 (2010).
[3]D. S. Meyaard, G. B. Lin, Q. Shan. J. Cho, E. F. Schubert, H. Shim, M. H. Kim, and Ch. Sone, Appl. Phys. Lett. **99**, 251115 (2011).
[4]J. Hader, J. V. Maloney, and S. W. Koch, Appl. Phys. Lett. **96**, 221106 (2010).
[5]T. Malinauskas, A. Kadys, T. Grinys, S. Nargelas, R. Aleksiejūnas, S. Miasojedovas, J. Mickevičius, R. Tomašiūnas, K. Jarašiūnas, M. Vengris, S. Okur, V. Avrutin, X. Li, F. Zhang, Ü. Özgür, and H. Morkoç, Proc. SPIE **8262**, 82621S (2012).
[6]A. Kaneta, M. Funato, and Y. Kawakami, Phys. Rev. B **78**, 125317 (2008).
[7]E. A. Oliver, S. E. Bennet, T. Zhu, D. J. Beesley, M. J. Kappers, D. W. Saxey, A. Cerezo, and C. J. Humphreys, J. Phys. D: Appl. Phys. **43**, 354003 (2010).
[8]S. F. Chichibu, A. Uedono, T. Onuma, B. A. Haskell, A.Chakraborty, T. Koyama, P. T. Fini, S. Keller, S. P. Denbaars, J. S. Speck, U. K. Mishra, S. Nakamura, S. Yamaguchi, S. Kamiyama. H. Amano, I. Akasaki, J. Han, and T. Sota, Nature Mater. **5**, 810 (2006).
[9]K. Jarašiūnas, R. Aleksiejūnas, T. Malinauskas, M. Sūdžius, S.Miasojedovas, S. Juršėnas, A. Žukauskas, R. Gaska, J. Zhang, M. S. Shur, J. W. Wang. E. Kuokštis, and M. A. Khan, Phys. Status Solidi A **202**, 820 (2005).
[10]P. Ščajev, K. Jarašiūnas, S. Okur, Ü. Özgür, and H. Morkoç, J. Appl. Phys. **111**, 023702 (2012).
[11]J. S. Im, A. Moritz, F. Steuber, V. Härle, F. Scholtz, and A. Hangleiter, Appl. Phys. Lett. **70**, 631 (1997).
[12]C. Netzel, V. Hoffman, T. Wernicke, A. Knauer, M. Weyers, M. Kneissl, and N. Szabo, J Appl. Phys. **107**, 033510 (2010).
[13]S. Miasojedovas, S. Juršėnas, A. Žukauskas, V. Yu. Ivanov, M. Godlewski, M. Leszczynski, P. Perlin, and T. Suski, J. Cryst. Growth **281**, 183 (2005).
[14]R. W. Martin, P. G. Middleton, and K. P. O'Donnell, Appl. Phys. Lett. **74**, 263 (1999).
[15]A. Satake, Y. Masumoto, T. Miyajima, T. Asatsuma, F. Nakamura, and M. Ikeda, Phys. Rev. B **57**, R2041 (1998).
[16]A. David and M. J. Grundman, Appl. Phys. Lett. **96**, 103504 (2010).
[17]H. J. Eichler, P. Gunter, and D. W. Pohl, *Laser-Induced Dynamic Gratings* (Springer, Berlin, 1986).
[18]K. Jarašiūnas, Proc. SPIE **7937**, 79371W (2011).
[19]T. Malinauskas, K. Jarašiūnas, M. Heuken, F. Scholz, and P. Bruckner, Phys. Status Solidi C **6**, S743 (2009).
[20]K. Jarašiūnas and H. J. Gerritsen, Appl. Phys. Lett. **33**, 190 (1978).
[21]T. Malinauskas, R. Aleksiejūnas, K. Jarašiūnas, B. Beaumont, P. Gibart, A. Kakanakova, E. Janzen, D. Gogova, B. Monemar, and M. Heuken, J. Cryst. Growth **300**, 223 (2007).
[22]P. Ščajev, A. Usikov, V. Soukhoveev, R. Aleksiejūnas, and K. Jarašiūnas. Appl. Phys. Lett. **98**, 202105 (2011).

[23]T. Malinauskas, K. Jarašiūnas R. Aleksiejunas, D. Gogova, B. Monemar, B. Beaumont, and P. Gibart, Phys. Status Solidi B **243**, 1426–1430 (2006).
[24]X. Li, S. Okur, F. Zhang, V. Avrutin, Ü. Özgür, H. Morkoç, S. M. Hong, S. H. Yen, T. C. Hsu, and A. Matulionis, J. Appl. Phys. **111**, 063112 (2012).
[25]J.-I. Shim, H. Kim, D.-S. Shin, and H.-Y. Ryu, J. Korean Phys. Soc. **58**, 503 (2011).
[26]Power index β of $I_{PL} \propto {I_0}^{\beta}$ dependence is doubled with respect to index γ of $I_{DT} \propto {I_0}^{\gamma}$ dependence because of bimolecular origin of photoluminescence ($\beta = 2\gamma$).
[27]L. Bellaiche, T. Matilla, L.-W. Wang, S.-H. Wei, and A. Zunger, Appl. Phys. Lett. **74**, 1842 (1999).
[28]C. Persson, U. Lindefelt, and B. E. Sernelius, Solid State Electron. **44**, 471 (2000).